

Geophysical Research Letters[®]

RESEARCH LETTER

10.1029/2021GL095024

Key Points:

- We find a heterogeneous, up to 5 km wide low-velocity zone around the 2019 Ridgecrest earthquake sequence using ambient noise tomography
- The locally sparse imaging technique better predicts travel times than conventional regularized least squares inversion
- Correlation of the low velocity zone with observed distributed faulting suggests an origin as fault damage zones

Supporting Information:

Supporting Information may be found in the online version of this article.

Correspondence to:

Z. Zhou,
zhz039@ucsd.edu

Citation:

Zhou, Z., Bianco, M., Gerstoft, P., & Olsen, K. (2022). High-resolution imaging of complex shallow fault zones along the July 2019 Ridgecrest ruptures. *Geophysical Research Letters*, 49, e2021GL095024. <https://doi.org/10.1029/2021GL095024>

Received 27 JUN 2021
Accepted 10 DEC 2021

High-Resolution Imaging of Complex Shallow Fault Zones Along the July 2019 Ridgecrest Ruptures

Zheng Zhou¹ , Michael Bianco¹, Peter Gerstoft¹ , and Kim Olsen²

¹University of California, San Diego, CA, USA, ²San Diego State University, San Diego, CA, USA

Abstract We perform ambient noise tomography using data recorded on 342 seismographs within a 50 × 50 km area inside which the July 2019 M7.1 and M6.4 Ridgecrest earthquakes occurred. We used the locally sparse tomography (LST) method, an unsupervised machine learning approach that learns to represent small-scale geophysical structures using only data from the immediate study. The Rayleigh group speed obtained from LST better predicts travel times than conventional regularized least squares inversion. The 3D shear velocity model of the area obtained from the surface wave dispersion maps reveals a highly heterogeneous low-velocity zone (with the primary velocity reduction in the upper 2–3 km) around the causative faults for the M7.1 and M6.4 events, with a 40% reduction of the shear wave velocity. Further, correlation of other imaged LVZs in the model area with parts of the Little Lake Fault System without recent activity may indicate long-lasting damage zones.

Plain Language Summary We perform ambient noise tomography in the region surrounding the surface ruptures of the 2019 Ridgecrest M7.1 and M6.4 earthquakes. The imaging method uses locally sparse tomography (LST), a machine learning-based method that directly learns the seismic travel time information from the data obtained from a coarse regional array and several dense arrays, with 342 seismic stations in total. The Rayleigh group speed obtained from LST outperforms the conventional regularized least-squared inversion in travel time predictions and provides more details of the small-scale geophysical structure. The 3D shear wave velocity model resulting from our imaging reveals a low velocity zone (LVZ) up to 5 km in width and ~5 km deep surrounding the surface expressions of the 2019 Ridgecrest earthquakes. The average velocity inside the LVZ is 40% lower than that for the surrounding material. The relatively wide LVZ obtained from our imaging is strongly correlated with the distributed faulting from geological and geodetic observations, suggesting an origin as fault damage zones. We find correlation of other imaged LVZs in the model area with faults that have not experienced recent activity. Therefore, if these LVZs represent fault damage zones, they may have persisted for hundreds, maybe thousands of years.

1. Introduction

On 4 July 2019, a M 6.4 earthquake occurred just northeast of the city of Ridgecrest, California, followed by a M 7.1 earthquake nearly 34 hr later on 6 July 2019 (Ross et al., 2019). The Ridgecrest sequence occurred within the Airport Lake and Little Lake Fault zones (Hernandez & Dawson, 2019) in the Eastern California Shear Zone (ECSZ), which accommodates 20%–25% of the Pacific-North America plate motion (Liu et al., 2010). The ECSZ has a long history of earthquake activity, featuring multiple seismic sequences with mainshock magnitude greater than 5 between 1982 and 1996 (Ross et al., 2019). The M 7.1 Ridgecrest earthquake was the largest earthquake to occur in ECSZ and southern California since the 1999 M 7.1 Hector Mine earthquake (Cochran et al., 2020).

Conventional 3D and machine learning-based 2D surface wave tomography are used to obtain a data-driven velocity model which helps illuminate the extent of the fault zone damage. Geological mapping studies (e.g., Hough et al., 2020) find extensive distributed faulting in a zone several kilometers wide around the 2019 Ridgecrest ruptures. While, the depth extent is unknown, we assume that this documented off-fault deformation in Ridgecrest is the surface expression of underlying fault damage characterized by a low-velocity zone (LVZ).

Accurate assessment of such fault zone damage is important for many applications, including earthquake location and seismic hazard analysis. For example, impedance effects and trapped waves in fault zones can cause ground motion amplification (e.g., Li & Leary, 1990; Parker et al., 2020), and rupture dynamics simulations suggest fault zones can affect the rupture pulse (e.g., Harris & Day, 1997) and cause super-shear rupture (e.g., Gabriel et al., 2012). Furthermore, nonlinear rheology in the fault zone may affect the rise time and shape of the rupture

pulse (Ben-Zion & Huang, 2002). Thus, accurate delineation of fault zone structure may improve seismic hazard analysis and fault plane delineation.

Fault damage zones are characterized by their depth-dependent width and velocity reduction relative to the surrounding material. Their dimensions and velocity reduction are estimated from the damage zone's effect on seismic wave propagation. For example, Li et al. (1990); Li and Vidale (1996); Li et al. (2004) used trapped waves from explosions and earthquakes to delineate the San Andreas fault zone. Tomographic inversion using earthquake arrival times can characterize velocity structure around mapped faults, such as the San Jacinto fault (Allam et al., 2014). In addition, fault zone imaging has used body wave travel times from local and teleseismic earthquakes (Yang et al., 2020), waveform modeling of trapped waves and body waves (Qin et al., 2018), and modeling diffracted S-waves around the LVZs (Y. Wang et al., 2019). However, while providing important constraints on the fault zone parameters, these methods generate poor resolution in the top 1–2 km due to predominantly deeper ray paths.

In this study we perform ambient noise tomography (ANT) of the Ridgecrest region. Ambient noise is a reliable tool for seismic imaging of Earth's crust, due to the abundance of shallow surface waves. Cross-correlations of noise obtained between station pairs provide estimates of group or phase velocities of the intervening media. The accuracy of the ANT depends on the spacing of the virtual-source receiver pairs. Deployments of dense seismic arrays with properly selected frequency bands have provided particularly high resolution measurements for recent near surface tomography studies (e.g., Bianco et al., 2019; Zigone et al., 2015; Zigone et al., 2019). Rayleigh waves, with prominent signature on vertical-component records, are sufficient to obtain the travel-time measurements between station-pairs. The ambient noise cross-correlation leads to depth-dependent velocity structure using surface wave dispersion inversion (e.g., Bowden et al., 2015; Lin et al., 2013).

The depth resolution of tomography depends on the frequency range used. We apply ambient noise correlation techniques to a rich data set collected during 58 days in 2019 (07/13–09/08), consisting of a combination of a coarse regional deployment and dense 2D arrays across the M6.4 and M7.1 July 2019 Ridgecrest surface ruptures (Catchings et al., 2020). Specifically, we estimate the S-wave velocity structure to 1 km depth using 0.02–1 Hz Rayleigh waves. Group travel-times are extracted from narrow band cross-correlation peaks. From these, 2D Rayleigh wave velocity models are estimated. Surface-wave dispersion analysis across a broad frequency range is then carried out at each grid point providing a local shear wave profile using a fully nonlinear direct-search algorithm (Julià et al., 2000). Finally, we stack the resulting S-wave profiles to construct a 3D S-wave model from the surface to a depth of 5 km.

Typically, ANT is performed using regularized least squares and travel-time residuals or Eikonal equation inversion (e.g., Lin et al., 2009). Recently, probabilistic neural network (Earp & Curtis, 2020), random mesh projection (Kothari & Gupta, 2019) and dictionary learning (Aghamiry & Gholami, 2018; Bianco & Gerstoft, 2018) have been used to generate the velocity models. Bianco and Gerstoft (2018) proposed improving tomography models by incorporating unsupervised machine learning. The method, locally sparse travel time tomography (LST), was demonstrated on a Nodal seismic array data set from Long Beach, CA 2011 (Bianco et al., 2019). The LST approach separates the overall or *global* tomography map into patches of small-scale or *local* variation, and considers the local and global information separately (Bianco & Gerstoft, 2018). LST, via sparse modeling, is capable of resolving sharp as well as smooth Earth features based on the data. Using the method for fault-zone imaging studies has potential to improve resolution, for example, at the boundaries of the LVZ, over conventional tomography approaches. We resample the travel times using cross-validation resampling to compare two ANT approaches: LST and Gaussian smoothing-kernel regularized least squares (LSQ) tomography (Equation S7 in Supporting Information S1). For both approaches, the parameters are chosen to minimize the travel time residual on withheld data (data not used to calculate model parameters).

2. Data Processing and Methodology

2.1. Data

We used the continuous seismic records (500 Hz sampling rate) from 07/13/2019 to 09/08/2019 around the Ridgecrest area by Catchings et al. (2020) on 342 seismic sensors, including 65 nodes in a regional array with 8–15 km spacing and 277 nodes in 6 dense arrays with 60–170 m spacing (A1, A2, and B1–B4 in Figure 1a). All

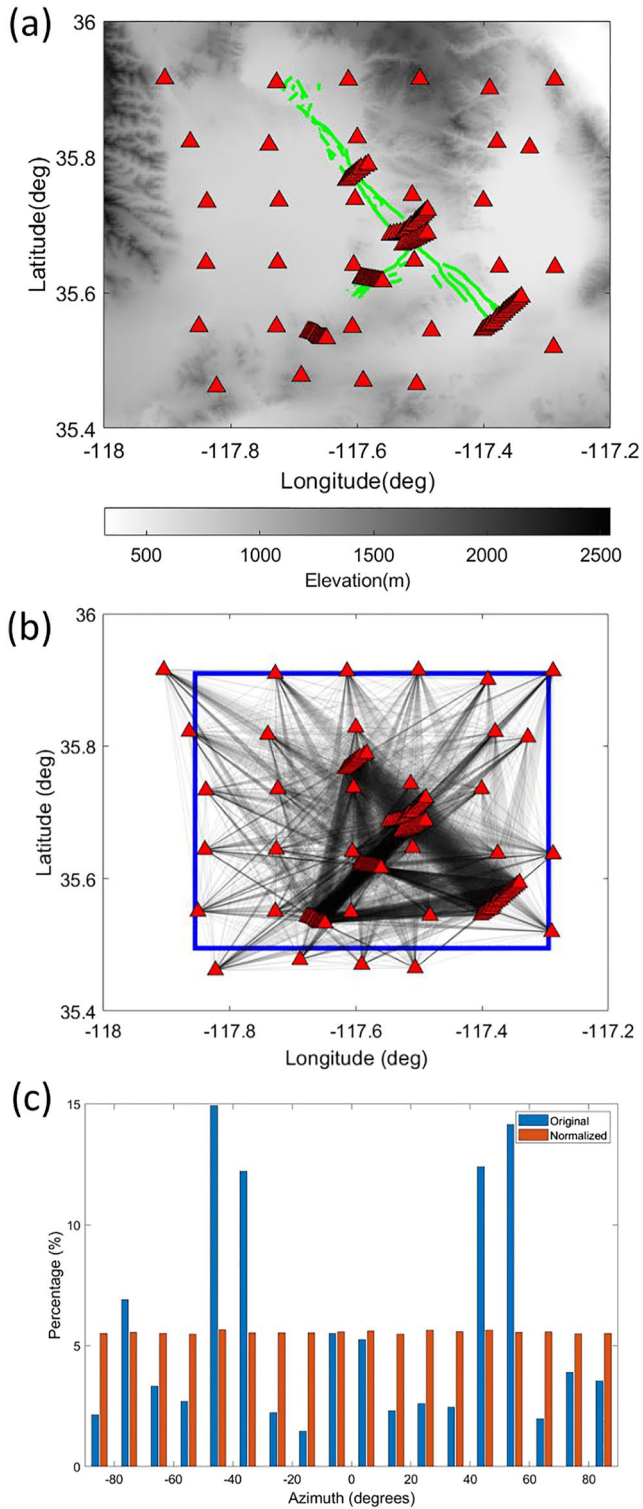


Figure 1. (a) Station locations (red triangles) and fault traces (green lines), (b) ray coverage in the model region (blue box), and (c) histogram of ray azimuths for the original and normalized distributions.

seismic data are from the FDSN 3J network (for an example of the seismic data and its spectrogram, see Figure S2 in Supporting Information S1).

2.2. Noise Tomography With Locally Sparse Model

We first bandpass-filtered the data using a 0.02–1.00 Hz 2nd-order Butterworth filter and down-sampled the records to a 5 Hz sampling rate. An amplitude truncation technique was applied for removal of aftershocks (Gerstoft et al., 2006), and spectral whitening (e.g., Roux et al., 2005) was then used to create data with a uniform amplitude spectrum. The data from every station pair were cross-correlated segment by segment, and the resulting correlograms were stacked over 6-hr intervals. Finally, a thresholding policy was adopted for quality control (see Section S1 in Supporting Information S1 for more details).

In conventional tomography, the least squares fit between observed and calculated travel times is minimized with regularization from the smoothness prior. Here, the slowness pixels are represented by the vector $\mathbf{s}' = \mathbf{s}_0 + \mathbf{s}_g \in R^N$, where \mathbf{s}_0 is a reference slowness and \mathbf{s}_g is a perturbation from the reference. The travel time observations are $\mathbf{t}' = \mathbf{t}_0 + \mathbf{t}_g \in R^N$, where \mathbf{t}_0 and \mathbf{t}_g are the reference travel times and perturbations. Since the reference slowness \mathbf{s}_0 is known, the reference travel time \mathbf{t}_0 is $\mathbf{t}_0 = \mathbf{A}\mathbf{s}_0$, where $\mathbf{A} \in R^{M \times N}$ denotes the tomography matrix. We estimate the perturbations by

$$\mathbf{t} = \mathbf{A}\mathbf{s}_g + \epsilon, \quad (1)$$

where, $\epsilon \in R^M$ is noise.

As a refinement of conventional tomography, LST introduces an additional slowness vector $\mathbf{s}_s \in R^N$, which captures the local slowness features (Bianco & Gerstoft, 2018) using sparse modeling and dictionary learning. Here, $\mathbf{D} \in R^{n \times Q}$ is a dictionary of Q atoms, and $\mathbf{x}_i \in R^n$ are the sparse coefficients with n being the number of pixels in a patch. R is a binary matrix which selects a particular patch from \mathbf{s}_g , and the Bayesian maximum a posteriori estimations $\{\hat{\mathbf{s}}_g, \hat{\mathbf{s}}_s, \hat{\mathbf{X}}\}$ are formulated as

$$\begin{aligned} \{\hat{\mathbf{s}}_g, \hat{\mathbf{s}}_s, \hat{\mathbf{X}}, \mathbf{D}\} = \underset{\mathbf{s}_g, \mathbf{s}_s, \mathbf{X}, \mathbf{D}}{\operatorname{argmin}} \left\{ \|\mathbf{w}(\mathbf{t} - \mathbf{A}\mathbf{s}_g)\|_2^2 + \lambda_1 \|\mathbf{s}_s - \mathbf{s}_g\|_2^2 \right. \\ \left. + \lambda_2 \sum_i \|\mathbf{D}\mathbf{x}_i - \mathbf{R}_i\mathbf{s}_g\|_2^2 \right\} \end{aligned} \quad (2)$$

$$\text{subject to } \|\mathbf{x}_i\|_0 = T \quad \forall i,$$

with, $\hat{\mathbf{X}} = [\hat{\mathbf{x}}_1, \dots, \hat{\mathbf{x}}_l]$ and λ_1, λ_2 are hyperparameters. The dictionary \mathbf{D} is learned during the optimization to represent local geophysical features with the sparse model. \mathbf{w} is a weight matrix which normalizes the biased ray-azimuth distribution. Such normalization is necessary because the seismic stations within the deployment of coarse regional and dense 2D arrays (Figure 1b) are highly unevenly distributed, causing a significant bias of the the ray-path with certain azimuths. The normalization term \mathbf{w} generates an unbiased azimuth distribution among the stations involved in our imaging (see Figure 1c). We set $l = 10$ pixels (corresponding to ~ 4 km) as our patch size, and $\lambda_1 = 1.58$ and $\lambda_2 = 0.40$ are the optimal hyperparameters picked from cross-validation tests (see Section 3 and the Supporting Information S1).

3. Cross-Validation: Model Selection

Fixed training datasets can be subdivided or resampled to obtain statistics of the data and models designed to explain them (Hastie et al., 2009). Cross-validation is one such technique, which is often used for selecting parameters for a model based on its performance on unseen samples (Raschka, 2018). In cross-validation, a given data set is divided into multiple training and validation datasets, called folds. The model weights are estimated using the training data, and its performance is evaluated on the validation set for each fold. The purpose of this test is to evaluate the model's ability to predict new data that was not used for training, over a sequence of different subdivisions of the data. This approach provides insight on the model's generalization to unseen data samples, and can indicate if the model is over- or underfitting the training data. In this work, models are chosen based on minimum average error on the validation set over the individual folds. Furthermore, the velocity models from the individual folds are used to obtain model uncertainty.

To evaluate the quality of velocity models obtained by the LST algorithm, we compare results from the LST method along with the LSQ tomography method (Rodgers, 2000).

Both LST and LSQ methods are used with a 10-fold cross-validation—we evenly sampled the station-wise travel time pairs into 10 folds and the sampled data in each fold have the same azimuth distribution (see Figure 1c) as the original data to avoid any direction-based bias. The LSQ model is solved assuming a constant reference velocity. The LST models are initialized using either a constant reference velocity, or the LSQ velocity model. The LST dictionary is initialized using Gaussian random atoms. Then, our LST and LSQ models are iteratively trained on 9-fold data and tested on the remaining fold. Our tests are performed on 0.7–0.9 Hz, 0.5–0.7 Hz, and 0.2–0.5 Hz data and we use the normalized travel time residual (NTTR) as the evaluation loss

$$loss_{NTTR} = \|\mathbf{w}(\mathbf{t} - \hat{\mathbf{t}})\|_2^2 = \sqrt{\sum_i \mathbf{w}_i(\mathbf{t}_i - \hat{\mathbf{t}}_i)^2}, \quad (3)$$

where, \mathbf{w} is the direction normalization vector for each fold, \mathbf{t} is the observed real travel time vector, and $\hat{\mathbf{t}} = \mathbf{A}\mathbf{s}$, is the predicted travel time vector from tomography results. \mathbf{w}_i , \mathbf{t}_i and $\hat{\mathbf{t}}_i$ are the i -th elements in \mathbf{w} , \mathbf{t} and $\hat{\mathbf{t}}$.

We summarize the averaged (mean) and the standard deviation of the Rayleigh group velocity (inverse slowness) maps for the 10-fold tests in different frequency bands in Figure 2a–b, and the 10-fold mean and standard deviation of the NTTR losses in Figure 2c. Lower averaged loss indicates tomography maps which better predicted the travel time, and lower loss variance denotes higher confidence and more stable results. The LST method outperforms conventional LSQ on these terms. Initializing the LST learning algorithm with a good prior, which starts the learning algorithm closer to the optimal solution, can further improve the travel time residuals (see Figure 2a). The lower frequency band corresponds to deeper velocity structure. We observe that the average velocity increases and the width of the LVZs shrinks as the sensitivity zone goes deeper. Generally, the LST provides lower velocities inside the LVZs, which results in a stronger contrast between the LVZs and the surrounding areas, and also sharpens the boundaries of the LVZs. Since each fold-test drops 10% of the ray paths randomly, the smaller standard deviation indicates that the LST model can provide results with higher confidence and stability (see Figure 2b).

4. 2D Ambient Noise Tomography

Figure 3a shows the Rayleigh group velocity map generated by the averaged 10-fold cross-validation tests on LST, representing a depth-average captured by the resolution kernel for 0.02–1 Hz, namely the upper ~1 km. The image shows relatively disjoint and spatially complex low-velocity regions on the map, in particular surrounding the surface rupture of the M7.1 and M6.4 Ridgecrest earthquakes. The average velocities of the surrounding material and the low-velocity zones are 2.8 and 1.7 km/s, respectively, and the width of these zones vary from 0 to 5 km.

The phase gradients mapped from daily passes of the Sentinel satellites (Milliner & Donnellan, 2020) are superimposed on the group velocity map in Figure 3a, indicating distributed faulting from the 2019 Ridgecrest events. There is a strong correlation between the LVZs and these phase gradients, suggesting that the distributed faulting occurred inside a kilometer-wide deformation zone.

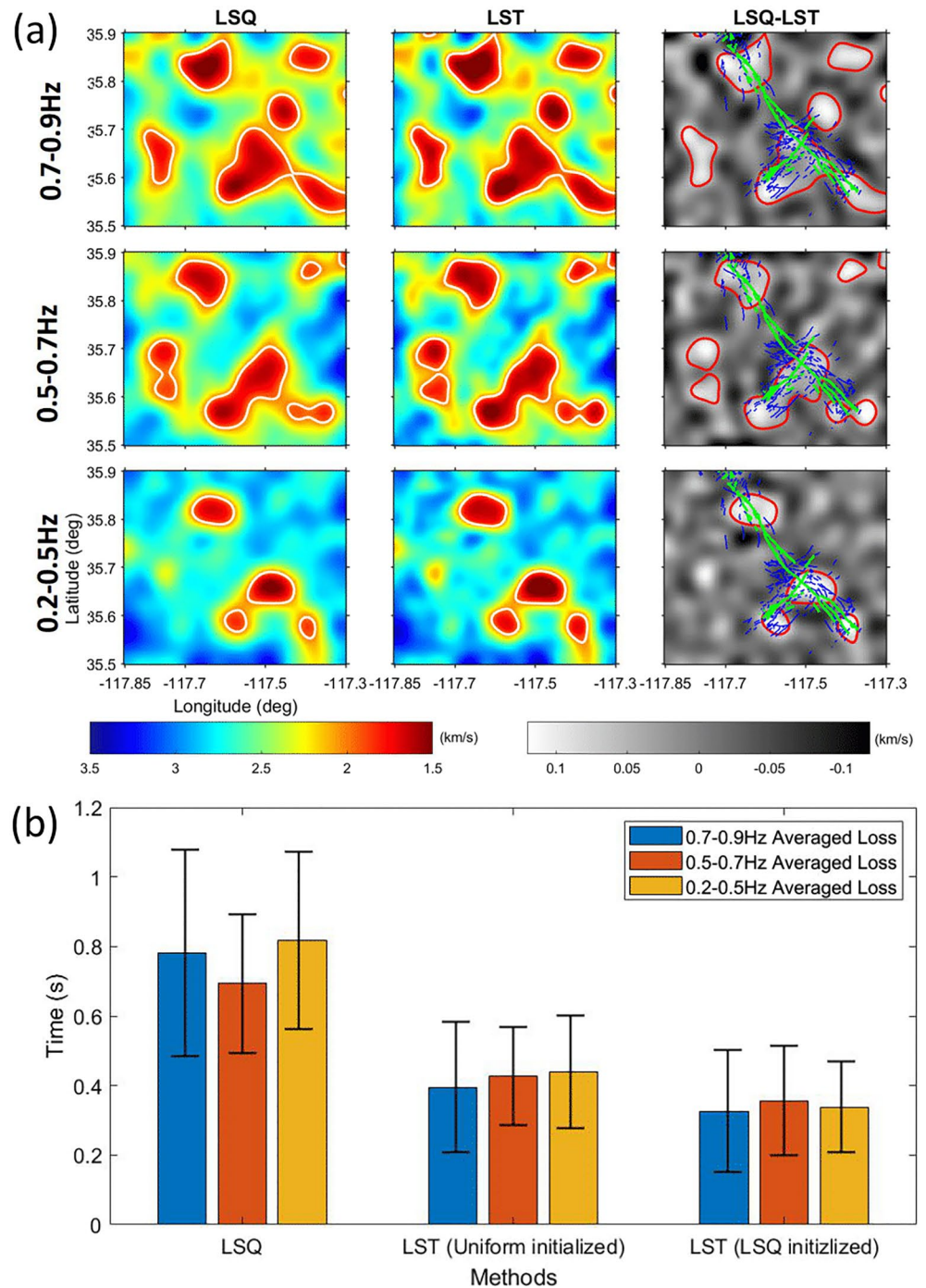


Figure 2. (a) 10 fold-averaged Rayleigh wave group velocity maps using least square (LSQ) and locally sparse tomography (LST) methods for 0.7–0.9, 0.5–0.7, and 0.2–0.5 Hz with the 2 km/s contour lines (white) superimposed. The LST is initialized by the least-square results. The difference maps (LSQ-LST) are superimposed with fault traces from field mapping (green lines), phase gradients of the Sentinel1 radar satellite (blue traces), and the 2 km/s Rayleigh wave velocity contour lines from the LST maps. (b) 10 fold-averaged mean (bins) and standard deviation (errorbars) of the normalized travel time residual losses derived by the LSQ and LST, which were initialized by either uniform or LSQ-estimated velocities.

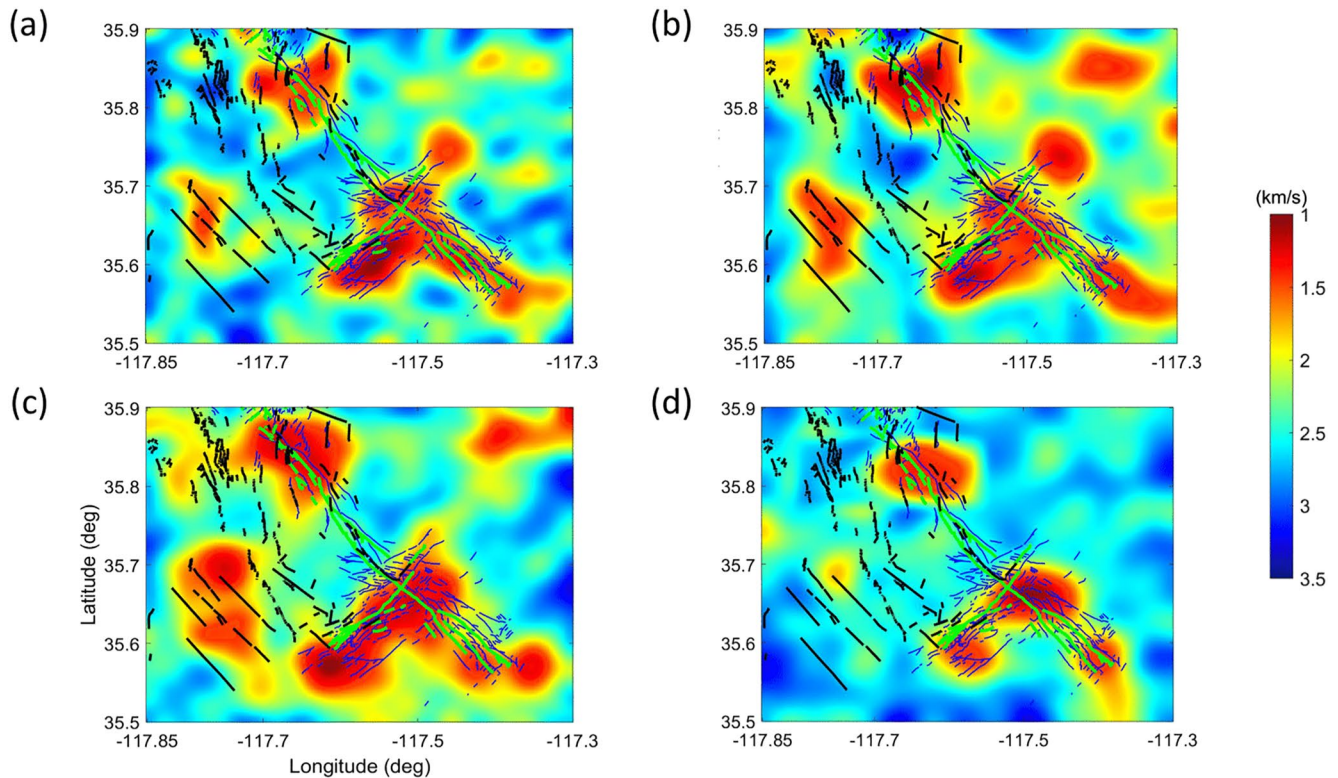


Figure 3. Rayleigh wave group velocity maps obtained using locally sparse tomography for bandwidths (a) 0.02–1, (b) 0.7–0.9, (c) 0.5–0.7, and (d) 0.2–0.5 Hz with superimposed fault traces that ruptured in the 2019 sequence (green lines), other Quaternary faults (black lines) and Sentinel1 phase gradients (blue traces). The velocity models are averaged over cross-validation folds. See also Figure S4 in Supporting Information S1.

Based on the Rayleigh wave group velocity resolution kernels, each frequency band senses different depths of the the shear wave velocity (Herrmann, 2013). For the bands in Figure 3c–3d the peak depths are 300 m (0.7–0.9 Hz), 450 m (0.5–0.7 Hz), and 700 m (0.2–0.5 Hz). Notice that the average velocity of the LVZs decrease/width of the LVZs shrinks as the depth increases, in agreement with the expected localization at greater depth found by other fault zone studies such as Zigone et al. (2015); Zigone et al. (2019).

5. Surface Wave Dispersion Inversion

The Rayleigh wave group velocities obtained by cross-correlation of ambient noise at each station pair are used to estimate group velocity dispersion curves. We use the fundamental mode dispersion curves picked in the frequency range of 0.1–3.0 Hz, and the estimated group velocities are inverted for a 1D shear-wave profile using a stochastic damped least squares inversion that minimizes the L2 norm misfit between synthesized and observed data (We use the SURF96 program (Herrmann, 2013). Examples of dispersion curves and the resulting S-wave profile are shown in Figure S3 in Supporting Information S1.). The technique (Herrmann, 2013) allows for the evaluation of partial derivatives of the Rayleigh wave group velocities with respect to the S-wave velocity and density for each layer. The model parameters are iteratively perturbed from the initial guess with a starting model taken from the Southern California Earthquake Center Community Velocity Model Version S-4.26 (Magistrale et al., 1996), which generally converges after a few iterations. The shear velocity profile is estimated for station pairs generated by every other station. The regions on either side of the surface rupture are modeled separately because of differences in the elevation of the stations (low elevations on the western side and high elevations on the eastern side).

Figure 4a shows cross sections of shear wave velocities from the inverted surface wave dispersion curves at the dense arrays A1, A2, B1, B2, B3, and B4, and a composite 3D image of shear wave velocities obtained by the sparse arrays is shown in Figure 4b. We observe relatively wide LVZs in the upper 1 km range of Figures 4a and 4b in our LST results. The surface traces from the M6.4 and M7.1 Ridgecrest events intersect the cross

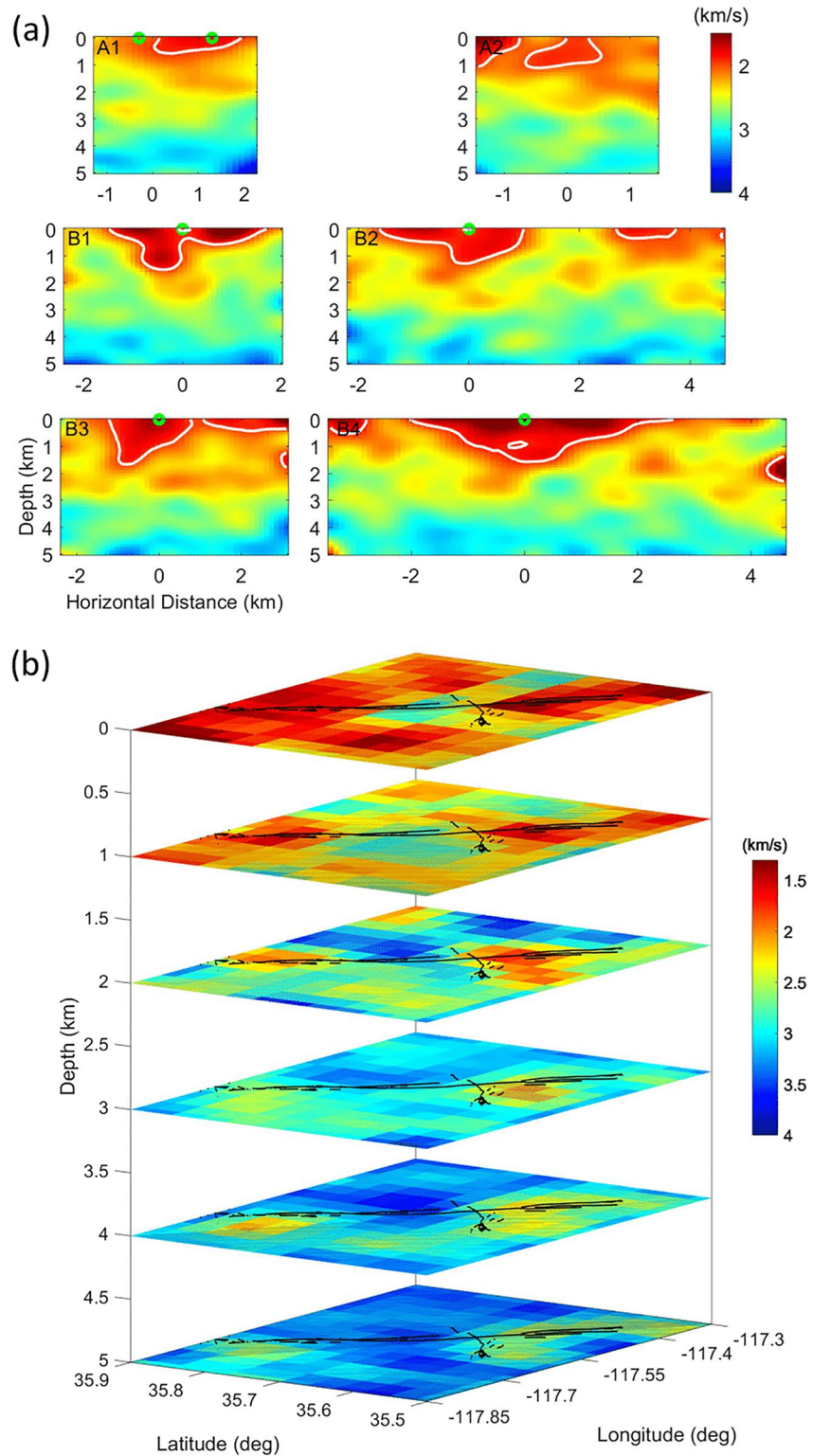


Figure 4. (a) Vertical cross section of the shear wave velocities from the A1, A2, B1, B2, B3, and B4 station arrays. The intersection with the surface rupture of the M6.4 and M7.1 Ridgecrest events (green circles) and 2 km/s contours (white lines) are indicated. (b) Composite 3D image of shear wave velocities obtained from inversion of Rayleigh waves dispersion curves, delineating flower-shaped low-velocity zones.

sections near the center of the LVZs, and the shallow cross sections reveal distinct LVZ flower structures, as observed by Zigone et al. (2019). However, the complexity of the fault zone, as characterized from the variation of particularly the width of the LVZ, is remarkable. For example, the fault zone at arrays A1 and B1 appear to delineate two or more separate low-velocity parts of the fault zone, which may represent a concentration of damage along different locations of the rupture for past events.

6. Discussion and Conclusions

Our tomographic model of the Ridgecrest area obtained using ambient noise and the LST approach resolves up to 5 km-wide flower-shaped LVZs with a velocity contrast of 40% to the host rock. The imaged LVZs are intersected by the fault traces of the M7.1 and M6.4 Ridgecrest events, suggesting an origin as a fault damage zone. It is unlikely that sedimentary deposits significantly contributed to the LVZs, which in several areas are located on topographic relief (refer to Figure 1a). In addition, the LVZs are relatively uncorrelated with depths to bedrock obtained from inversion of gravity data (Langenheim, 2019). We have shown that our LST method, by being primarily data-driven, can yield improved seismic velocity images over conventional approaches in terms of smaller predicted travel time residuals. We further obtained data-driven estimates of the model uncertainty with a cross-validation resampling method. It was observed that the model obtained with LST had lower uncertainty than that from regularized LSQ.

Our results are in general agreement with other imaging studies of fault zone structure (e.g., Ben-Zion et al., 1999; Lewis & Ben-Zion, 2010; Li & Vidale, 1996), including delay time analysis for the M7.1 Ridgecrest event (Qiu et al., 2021). Similarly, Antoine et al. (2021) found a 2–4 km wide fault zone along the M7.1 event using optical satellite image correlation. They also showed that slip associated with the M7.1 earthquake is caused by rupture on a complex set of primary fault segments and shallow (<2 km) surface diffuse deformation, with some inelastic contribution required to explain the latter. These findings are in agreement with the depth of primary velocity reduction in our imaging (see Figure 4), as well as the “flower-structure” of nonlinear deformation obtained by dynamic rupture simulations (Ma, 2008; Roten et al., 2018). Finally, the dimensions of our imaged LVZ in Ridgecrest are largely consistent with high-resolution seismic reflection imaging from the 2000 M6.7 Tottori, Japan, earthquake that revealed a 2 km-deep flower structure with several kilometer-wide surface extent (Nishitani & Inoue, 2001). The 2000 Tottori earthquake occurred on a near-vertical, shallow crustal strike-slip event, much like the M7.1 Ridgecrest event, with similar distributed faulting and surface cracks.

While the imaged LVZs along the M7.1 and M6.4 Ridgecrest fault traces may be solely explained by the 2019 sequence, our imaging reveals “pockets” of low velocity material outside the proposed damage zones for the 2019 Ridgecrest event (see Figure 3). The resolution of our results in these areas is degraded from limited ray coverage, and some of the low velocities may be caused by sediments. However, it is possible that these low velocities represent damage zones from past Quaternary earthquakes within the Little Lake Fault Zone located in the southwestern part of the model area (see Figure 3). Since, these faults have not experienced large historical events, the fault damage here may have persisted for hundreds, maybe thousands of years. The existence of such long-lasting damage zones agrees with results for the Calico fault zone (Cochran et al., 2009; Zhang & Gerstoft, 2014) and the San Jacinto Fault (Zigone et al., 2019), which implies relatively slow damage zone healing.

The shallow fault zone obtained from our surface wave dispersion is highly heterogeneous. Specifically, the imaged LVZ, as well as off-fault deformation from the mapped phase gradients from the Sentinel1 radar (see Figure 3), are largely missing along a ≈ 10 km stretch from the M7.1 epicenter toward the south to the intersection of the M6.4 earthquake. The lack of significant off-fault deformation in this area may be due a relatively section of the fault with large surface displacement as indicated by kinematic source inversions (e.g., K. Wang et al., 2020), accommodating most of the slip on the primary fault traces. Finally, the strong heterogeneity of the shallow fault zone obtained from our surface wave dispersion suggests an incipient fault zone, with multiple fault segments not optimally oriented for failure (Crider & Peacock, 2004), as found in other areas (e.g., Goldberg et al., 2020; Lomax, 2020; Shelly, 2020; Shi & Wei, 2020). Such regions are less likely to host large earthquakes, as compared to mature faults, for example, the San Andreas fault.

Data Availability Statement

The seismic data used in this paper are accessed from the FDSN 3J:RAMP deployment of 3C nodal for July Searles Valley 2019 Earthquake (doi: [10.7914/SN/3J_2019](https://doi.org/10.7914/SN/3J_2019)).

Acknowledgments

This research was supported by the Southern California Earthquake Center (SCEC Contribution Number 21133). SCEC is funded by National Science Foundation Cooperative Agreement EAR-1600087 and U.S. Geological Survey Cooperative Agreement G17AC00047.

References

- Aghamiry, H. S., & Gholami, A. (2018). Interval-Q estimation and compensation: An adaptive dictionary-learning approach. *Geophysics*, 83(4), V233–V242. <https://doi.org/10.1190/geo2017-0001.1>
- Allam, A., Ben-Zion, Y., Kurzon, I., & Vernon, F. (2014). Seismic velocity structure in the hot springs and trifurcation areas of the San Jacinto fault zone, California, from double-difference tomography. *Geophysical Journal International*, 198(2), 978–999. <https://doi.org/10.1093/gji/ggu176>
- Antoine, S. L., Klinger, Y., Delorma, A., Wang, K., Burgmann, R., & Gold, R. D. (2021). Diffuse deformation and surface faulting distribution from submetric image correlation along the 2019 Ridgecrest, California, ruptures. *Bulletin of the Seismological Society of America*, 111(5), 2275–2302.
- Ben-Zion, Y., Dahmen, K., Lyakhovskiy, V., Ertas, D., & Agnon, A. (1999). Self-driven mode switching of earthquake activity on a fault system. *Earth and Planetary Science Letters*, 172(1–2), 11–21. [https://doi.org/10.1016/s0012-821x\(99\)00187-9](https://doi.org/10.1016/s0012-821x(99)00187-9)
- Ben-Zion, Y., & Huang, Y. (2002). Dynamic rupture on an interface between a compliant fault zone layer and a stiffer surrounding solid. *Journal of Geophysical Research*, 107(B2). <https://doi.org/10.1029/2001jb000254>
- Bianco, M. J., & Gerstoft, P. (2018). Travel time tomography with adaptive dictionaries. *IEEE Transactions on Computational Imaging*, 4(4), 499–511. <https://doi.org/10.1109/tci.2018.2862644>
- Bianco, M. J., Gerstoft, P., Olsen, K. B., & Lin, F.-C. (2019). High-resolution seismic tomography of long beach, ca using machine learning. *Scientific Reports*, 9(1), 1–11. <https://doi.org/10.1038/s41598-019-50381-z>
- Bowden, D., Tsai, V. C., & Lin, F. C. (2015). Site amplification, attenuation, and scattering from noise correlation amplitudes across a dense array in long beach, ca. *Geophysical Research Letters*, 42(5), 1360–1367. <https://doi.org/10.1002/2014gl062662>
- Catchings, R. D., Goldman, M. R., Steidl, J. H., Chan, J. H., Allam, A. A., Criley, C. J., et al. (2020). Nodal seismograph recordings of the 2019 Ridgecrest earthquake sequence. *Seismological Research Letters*, 91(6), 3622–3633. <https://doi.org/10.1785/0220200203>
- Cochran, E. S., Li, Y.-G., Shearer, P. M., Barbot, S., Fialko, Y., & Vidale, J. E. (2009). Seismic and geodetic evidence for extensive, long-lived fault damage zones. *Geology*, 37(4), 315–318. <https://doi.org/10.1130/g25306a.1>
- Cochran, E. S., Wolin, E., McNamara, D. E., Yong, A., Wilson, D., Alvarez, M., et al. (2020). The U.S. geological survey's rapid seismic array deployment for the 2019 Ridgecrest earthquake sequence. *Seismological Research Letters*, 91(4), 1952–1960. <https://doi.org/10.1785/0220190296>
- Cridler, J. G., & Peacock, D. C. (2004). Initiation of brittle faults in the upper crust: A review of field observations. *Journal of Structural Geology*, 26(4), 691–707. <https://doi.org/10.1016/j.jsg.2003.07.007>
- Earp, S., & Curtis, A. (2020). Probabilistic neural network-based 2d travel-time tomography. *Neural Computing & Applications*, 32(22), 17077–17095. <https://doi.org/10.1007/s00521-020-04921-8>
- Gabriel, A.-A., Ampuero, J.-P., Dalguer, L. A., & Mai, P. M. (2012). The transition of dynamic rupture styles in elastic media under velocity-weakening friction. *Journal of Geophysical Research: Solid Earth*, 117(B9). <https://doi.org/10.1029/2012jb009468>
- Gerstoft, P., Sabra, K. G., Roux, P., Kuperman, W. A., & Fehler, M. C. (2006). Green's functions extraction and surface-wave tomography from microseisms in southern California. *Geophysics*, 71(4), SI23–SI31. <https://doi.org/10.1190/1.2210607>
- Goldberg, D. E., Melgar, D., Sahakian, V., Thomas, A., Xu, X., Crowell, B., & Geng, J. (2020). Complex rupture of an immature Fault zone: A simultaneous kinematic model of the 2019 Ridgecrest, ca earthquakes. *Geophysical Research Letters*, 47(3), e2019GL086382. <https://doi.org/10.1029/2019gl086382>
- Harris, R. A., & Day, S. M. (1997). Effects of a low-velocity zone on a dynamic rupture. *Bulletin of the Seismological Society of America*, 87(5), 1267–1280.
- Hastie, T., Tibshirani, R., & Friedman, J. (2009). *The elements of statistical learning: Data mining, inference and prediction* (2nd ed.). Springer.
- Hernandez, J. L., & Dawson, T. E. (2019). *Triggered slip on the little lake fault zone resulting from the 2019 Ridgecrest earthquake sequence, California*. AGUFM. S31F–0459.
- Herrmann, R. B. (2013). Computer programs in seismology: An evolving tool for instruction and research. *Seismological Research Letters*, 84(6), 1081–1088. <https://doi.org/10.1785/0220110096>
- Hough, S. E., Ross, Z. E., & Dawson, T. E. (2020). Introduction to the special section on the 2019 Ridgecrest, California, earthquake sequence. *Bulletin of the Seismological Society of America*, 110(4), 1395–1399. <https://doi.org/10.1785/0120200201>
- Julia, J., Ammon, C. J., Herrmann, R. B., & Correig, A. M. (2000). Joint inversion of receiver function and surface wave dispersion observations. *Geophysical Journal International*, 143(1), 99–112. <https://doi.org/10.1046/j.1365-246x.2000.00217.x>
- Kothari, K., & Gupta, S. (2019). Random mesh projectors for inverse problems. In *7th international conference on learning representations*. ICLR.
- Langenheim, V. E. (2019). *Setting of the Ridgecrest and Searles Valley earthquakes from gravity and magnetic data*. Geological Society of America Annual Meeting.
- Lewis, M. A., & Ben-Zion, Y. (2010). Diversity of fault zone damage and trapping structures in the Parkfield section of the San Andreas Fault from comprehensive analysis of near fault seismograms. *Geophysical Journal International*, 183(3), 1579–1595. <https://doi.org/10.1111/j.1365-246x.2010.04816.x>
- Li, Y.-G., & Leary, P. (1990). Fault zone trapped seismic waves. *Bulletin of the Seismological Society of America*, 80(5), 1245–1271. <https://doi.org/10.1785/bssa0800051245>
- Li, Y.-G., Leary, P., Aki, K., & Malin, P. (1990). Seismic trapped modes in the Oroville and San Andreas Fault zones. *Science*, 249(4970), 763–766. <https://doi.org/10.1126/science.249.4970.763>
- Li, Y.-G., & Vidale, J. E. (1996). Low-velocity fault-zone guided waves: Numerical investigations of trapping efficiency. *Bulletin of the Seismological Society of America*, 86(2), 371–378.
- Li, Y.-G., Vidale, J. E., & Cochran, E. S. (2004). Low-velocity damaged structure of the San Andreas Fault at Parkfield from fault zone trapped waves. *Geophysical Research Letters*, 31(12). <https://doi.org/10.1029/2003gl019044>
- Lin, F.-C., Li, D., Clayton, R. W., & Hollis, D. (2013). High-resolution 3D shallow crustal structure in Long Beach, California: Application of ambient noise tomography on a dense seismic array. *Geophysics*, 78(4), Q45–Q56. <https://doi.org/10.1190/geo2012-0453.1>

- Lin, F.-C., Ritzwoller, M. H., & Snieder, R. (2009). Eikonal tomography: Surface wave tomography by phase front tracking across a regional broad-band seismic array. *Geophysical Journal International*, 177(3), 1091–1110. <https://doi.org/10.1111/j.1365-246x.2009.04105.x>
- Liu, M., Wang, H., & Li, Q. (2010). Inception of the eastern California shear zone and evolution of the Pacific-North American plate boundary: From kinematics to geodynamics. *Journal of Geophysical Research*, 115(B7), B07401. <https://doi.org/10.1029/2009jb007055>
- Lomax, A. (2020). Absolute location of 2019 Ridgecrest seismicity reveals a shallow Mw 7.1 hypocenter, migrating and pulsing Mw 7.1 foreshocks, and duplex Mw 6.4 ruptures. *Bulletin of the Seismological Society of America*, 110(4), 1845–1858. <https://doi.org/10.1785/0120200006>
- Ma, S. (2008). A physical model for widespread near-surface and fault zone damage induced by earthquakes. *Geochemistry, Geophysics, Geosystems*, 9(11), Q11009. <https://doi.org/10.1029/2008gc002231>
- Magistrale, H., McLaughlin, K., & Day, S. (1996). A geology-based 3d velocity model of the Los Angeles basin sediments. *Bulletin of the Seismological Society of America*, 86(4), 1161–1166.
- Milliner, C., & Donnellan, A. (2020). Using daily observations from Planet Labs satellite imagery to separate the surface deformation between the 4 July Mw 6.4 foreshock and 5 July Mw 7.1 mainshock during the 2019 Ridgecrest earthquake sequence. *Seismological Research Letters*, 91(4), 1986–1997. <https://doi.org/10.1785/0220190271>
- Nishitani, A., & Inoue, Y. (2001). Overview of the application of active/semiaactive control to building structures in Japan. *Earthquake Engineering & Structural Dynamics*, 30(11), 1565–1574. <https://doi.org/10.1002/eqe.81>
- Parker, G. A., Baltay, A. S., Rekoske, J., & Thompson, E. M. (2020). Repeatable source, path, and site effects from the 2019 M 7.1 Ridgecrest earthquake sequence. *Bulletin of the Seismological Society of America*, 110(4), 1530–1548. <https://doi.org/10.1785/0120200008>
- Qin, L., Ben-Zion, Y., Qiu, H., Share, P., Ross, Z., & Vernon, F. (2018). Internal structure of the San Jacinto fault zone in the trifurcation area southeast of Anza, California, from data of dense seismic arrays. *Geophysical Journal International*, 213(1), 98–114. <https://doi.org/10.1093/gji/ggx540>
- Qiu, H., Ben-Zion, Y., Catchings, R., Goldman, M. R., Allam, A., & Steidl, J. (2021). Seismic imaging of the Mw 7.1 Ridgecrest earthquake rupture zone from data recorded by dense linear arrays. *Journal of Geophysical Research: Solid Earth*, 126(7), <https://doi.org/10.1029/2021jb022043>
- Raschka, S. (2018). *Model evaluation, model selection, and algorithm selection in machine learning*. arXiv preprint arXiv:1811.12808.
- Rodgers, D. (2000). *Inverse Methods for Atmospheric Sounding: Theory and Practice* (Vol. 2). World scientific.
- Ross, Z. E., Idini, B., Jia, Z., Stephenson, O. L., Zhong, M., Wang, X., et al. (2019). Hierarchical interlocked orthogonal faulting in the 2019 Ridgecrest earthquake sequence. *Science*, 366(6463), 346–351. <https://doi.org/10.1126/science.aaz0109>
- Roten, D., Olsen, K., Day, S., & Cui, Y. (2018). Quantification of fault-zone plasticity effects with spontaneous rupture simulations. In *Pure and Applied Geophysics*, 174(9), 3369–3391. <https://doi.org/10.1007/s00024-017-1466-5>
- Roux, P., Sabra, K. G., Gerstoft, P., Kuperman, W., & Fehler, M. C. (2005). P-waves from cross-correlation of seismic noise. *Geophysical Research Letters*, 32(19), L19303. <https://doi.org/10.1029/2005gl023803>
- Shelly, D. R. (2020). A high-resolution seismic catalog for the initial 2019 Ridgecrest earthquake sequence: Foreshocks, aftershocks, and faulting complexity. *Seismological Research Letters*, 91(4), 1971–1978. <https://doi.org/10.1785/0220190309>
- Shi, Q., & Wei, S. (2020). Highly heterogeneous pore fluid pressure enabled rupture of orthogonal faults during the 2019 Ridgecrest Mw7. 0 earthquake. *Geophysical Research Letters*, 47(20), e2020GL089827. <https://doi.org/10.1029/2020gl089827>
- Wang, K., Dreger, D. S., Tinti, E., Bürgmann, R., & Taira, T. (2020). Rupture process of the 2019 Ridgecrest, California Mw 6.4 foreshock and Mw 7.1 earthquake constrained by seismic and geodetic data. *Bulletin of the Seismological Society of America*, 110(4), 1603–1626. <https://doi.org/10.1785/0120200108>
- Wang, Y., Allam, A., & Lin, F.-C. (2019). Imaging the fault damage zone of the San Jacinto fault near anza with ambient noise tomography using a dense nodal array. *Geophysical Research Letters*, 46(22), 12938–12948. <https://doi.org/10.1029/2019gl084835>
- Yang, H., Duan, Y., Song, J., Jiang, X., Tian, X., Yang, W., & Yang, J. (2020). Fine structure of the Chenghai fault zone, yunnan, China, constrained from teleseismic travel time and ambient noise tomography. *Journal of Geophysical Research: Solid Earth*, 125(7), e2020JB019565. <https://doi.org/10.1029/2020jb019565>
- Zhang, J., & Gerstoft, P. (2014). Local-scale cross-correlation of seismic noise from the calico fault experiment. *Earthquake Science*, 27(3), 311–318. <https://doi.org/10.1007/s11589-014-0074-z>
- Zigone, D., Ben-Zion, Y., Campillo, M., & Roux, P. (2015). Seismic tomography of the southern California plate boundary region from noise-based Rayleigh and love waves. *Pure and Applied Geophysics*, 172(5), 1007–1032. <https://doi.org/10.1007/s00024-014-0872-1>
- Zigone, D., Ben-Zion, Y., Lehujeur, M., Campillo, M., Hillers, G., & Vernon, F. L. (2019). Imaging subsurface structures in the San Jacinto fault zone with high-frequency noise recorded by dense linear arrays. *Geophysical Journal International*, 217(2), 879–893. <https://doi.org/10.1093/gji/ggz069>